JGR Atmospheres

RESEARCH ARTICLE
10.1029/2021JD035531

Spatial Patterns of the Tropical Meridional Circulation: Drivers and Teleconnections

Eli Galanti[1], Dana Raiter[1], Yohai Kaspi[1], and Eli Tziperman[2]

[1]Department of Earth and Planetary Sciences, Weizmann Institute of Science, Rehovot, Israel, [2]Department of Earth and Planetary Sciences and School of Engineering and Applied Sciences, Harvard University, Cambridge, MA, USA

Key Points:

- Spatial patterns of the longitudinally dependent meridional circulation (LMC) found by clustering analysis, show zonal and meridional shifts
- El Niño-Southern Oscillation-driven Sea Surface Temperature is important in forcing the LMC variability, but the effect requires more than the standard Nino3.4 and Southern Oscillation indices
- LMC patterns are also driven by the Madden-Julian Oscillation, and affect other climatological variables such as remote surface air temperature and precipitation

Supporting Information:

Supporting Information may be found in the online version of this article.

Correspondence to:

E. Galanti,
eli.galanti@weizmann.ac.il

Citation:

Galanti, E., Raiter, D., Kaspi, Y., & Tziperman, E. (2022). Spatial patterns of the tropical meridional circulation: Drivers and teleconnections. *Journal of Geophysical Research: Atmospheres*, *127*, e2021JD035531. https://doi.org/10.1029/2021JD035531

Received 8 JUL 2021
Accepted 28 DEC 2021

Abstract The large-scale Hadley circulation is a key element in the global heat and moisture transport. It is traditionally defined as the zonally averaged meridional circulation in the tropics, but was shown to have a strong longitudinal dependence, as seen in a decomposition of the three-dimensional atmospheric flow into spatially dependent meridional and zonal circulations. Recent studies provided a useful analysis of the regional strengthening/weakening of the decomposed circulation but not its patterns. Here, we study the interannual variability of the longitudinally dependent meridional circulation (LMC), with a focus on its spatial patterns. We use hierarchical clustering to objectively determine the four main modes of the LMC interannual variability, and apply a Lagrangian air parcel tracking method to reveal the full circulation patterns. While El Niño and La Niña are found, as in previous studies, to play a role in setting these patterns, we find the patterns are not uniquely characterized by standard El Niño-Southern Oscillation (ENSO) indices (Nino3.4 or Southern Oscillation Index). Instead, ENSO flavors (i.e., East Pacific vs. Central Pacific) have different effects on the LMC. The most prominent interannual variability of the LMC is an east-west shift. Latitudinal shifts, as well as contraction/expansion in both latitude and longitude are also identified. Multiple linear regression analysis shows that while a large fraction of the LMC variance is explained by Sea Surface Temperature, the Madden-Julian Oscillation makes a nonnegligible independent contribution. The clustering patterns are also used to study the remote precipitation and surface air temperature teleconnections.

1. Introduction

The Hadley circulation is a key element of the climate system (Hartmann, 1994), responsible for the energy and moisture transport from the equatorial region to the subtropics (e.g., Trenberth & Stepaniak, 2003). The circulation is commonly defined as the zonally averaged meridional circulation in the tropical region (Hartmann, 2016), and is usually calculated as an annual mean or as an average over specific months or seasons.

The large longitudinal variations in the different elements involved in the Hadley circulation, such as the strength of the Inter Tropical Convergence Zone (ITCZ) and the location of the subtropical jets that mark the edges of the Hadley circulation, led to the need to calculate the contributions to the Hadley circulation at different longitudes. A method for calculating localized 2-D circulations from the 3-D wind field was first introduced by Keyser et al. (1989). Decomposing the wind field into a rotational and divergent components (Helmholtz decomposition), the longitudinally dependent circulation can be derived from the divergent part of the flow. This method was implemented in several studies for the analysis of the meridional and zonal circulations in specific longitudinal sectors. It was first used to define the horizontal velocity potential and divergent wind in the upper troposphere, in which both the meridional circulation and the zonal circulation are manifested. This definition enabled the investigation of the global monsoon system and its relation to the two circulations on seasonal to decadal time scales (Tanaka et al., 2004; Trenberth et al., 2000). The Helmholtz decomposition was also examined in comparison to a more general 3-D decomposition of global atmospheric circulation (Hu et al., 2017).

Motivated by indications that the extent and strength of the Hadley circulation exhibit natural variability (e.g., Simpson, 2018), and might change in the coming century (e.g., Chemke & Polvani, 2019; Grise et al., 2019; Held & Soden, 2006), Helmholtz decomposition was also used to examine the natural variability and decadal change of the longitudinally dependent meridional circulation (LMC) extent, either for specific sectors of the world (Nguyen et al., 2018), or directly as function of longitude (Staten et al., 2019). More recently, Raiter et al. (2020) used the same method, combined with a Lagrangian tracking of air parcels, to examine in detail the mean tropical

circulation, showing how the LMC acts together with the subtropical jets to produce a tropical atmospheric conveyor belt.

Decomposition of the flow field into local meridional and zonal circulations was used to calculate the relative contributions of the vertical mass fluxes in the middle-troposphere to the meridional and zonal cells (Schwendike et al., 2014). Note that in that study, as well as in other studies, the local circulations are referred as Hadley and Walker circulations. Here, we will use the more generic terms of meridional and zonal circulations, in order to avoid confusion with the classical definitions. The spatial distribution of vertical and meridional velocities were used also to calculate trajectories of climatological flow, emphasizing the regional aspects of the meridional circulation (Karnauskas & Ummenhofer, 2014). Examining the interannual variability of these two cells, Schwendike et al. (2014) found that the El Niño-Southern Oscillation (ENSO) has a much larger effect on the local meridional circulation than on the local zonal circulation. This study was performed over specific longitudinal and latitudinal sectors, focusing on the Maritime continent. The same methodology was later used to study the inter-decadal trend of both the meridional and zonal circulations (Schwendike et al., 2015), where it was shown that in order to understand the effect of climate variability on the tropical circulation patterns, the analysis should be regional. The longitudinally dependent circulations were also found to be correlated with different phases of the Madden-Julian Oscillation (MJO; Schwendike et al., 2021). The same method was also used to study specific regions of interest, such as the Atlantic sector of the meridional circulation during the boreal summer and its connection to the Atlantic tropical cyclone activity (Zhang & Wang, 2013).

The examination of the interannual variability of the large scale circulation in the above studies was mostly limited to the strengthening/weakening of the meridional (or zonal) circulation at different sectors of the world, with less emphasis on the spatial changes. Another limitation of past studies is the methodology used for investigating the interannual variability, which was defined based on other modes of variability in the tropical region, for example, a state of El Niño or a state of La Niña. This makes the variability of the meridional circulation a mere reflection of the other modes of variability. Therefore, there is a need to define the modes of interannual variability of the local meridional circulation with a more objective method.

Here we study the interannual variability of the LMC using clustering analysis, allowing an objective determination of the most important spatial pattens of variability. We then calculate the Sea Surface Temperature (SST) composites for each LMC pattern (cluster). While previous studies (e.g., Schwendike et al., 2014) examined the interannual variability of the LMC by calculating its composites for El Niño and La Niña states, our approach allows examining the connection to climate variability modes without assuming such a connection to start with. We also use the clustering patterns to characterize spatial shifts, widths and the spatial symmetry (skewness) of the LMC spatial patterns, and, their dependence on the SST. In addition, we use a Lagrangian perspective to tie these modes to the actual 3-D changes in the air flow. We use multiple linear regression analysis to link the LMC variability to the SST and the MJO, as well as to remote precipitation and surface air temperature patterns.

The manuscript is organized as follows: in Section 2, we present the method by which the local meridional circulation is calculated and the method for clustering its interannual variability. The results are shown in Section 3, with the characteristics of the LMC spatial patterns discussed in Section 3.1, and the relation to other climatic variables discussed in Section 3.2. We conclude in Section 4.

2. Data and Methods

2.1. The Longitudinally Dependent Meridional Circulation

We use three data sets to ensure robustness of our analysis: the European Center for Medium range Weather Forecasts ERA-Interim reanalysis (Dee et al., 2013), their newer ERA5 reanalysis (Hersbach et al., 2020), and the National Centers for Environmental Prediction (NCEP) reanalysis II (Kanamitsu et al., 2002). In our analysis we use the monthly mean data covering the years 1979–2018. All three data sets are used to perform the analysis, but in the results we show the ERA-Interim data. This data set was extensively used in recent studies discussing the large scale tropical circulation, especially in relation to the longitudinal variability, which is our focus here (e.g., Grise et al., 2019; Guo & Tan, 2018; Hu et al., 2017; Karnauskas & Ummenhofer, 2014; Nguyen et al., 2018; Schwendike et al., 2014; Schwendike et al., 2015; Schwendike et al., 2021). In order to make a meaningful and direct comparison to these works, we choose to use the same data set in the main text, but also show the results for the NCEP2 and ERA5 in the Supporting Information S1.

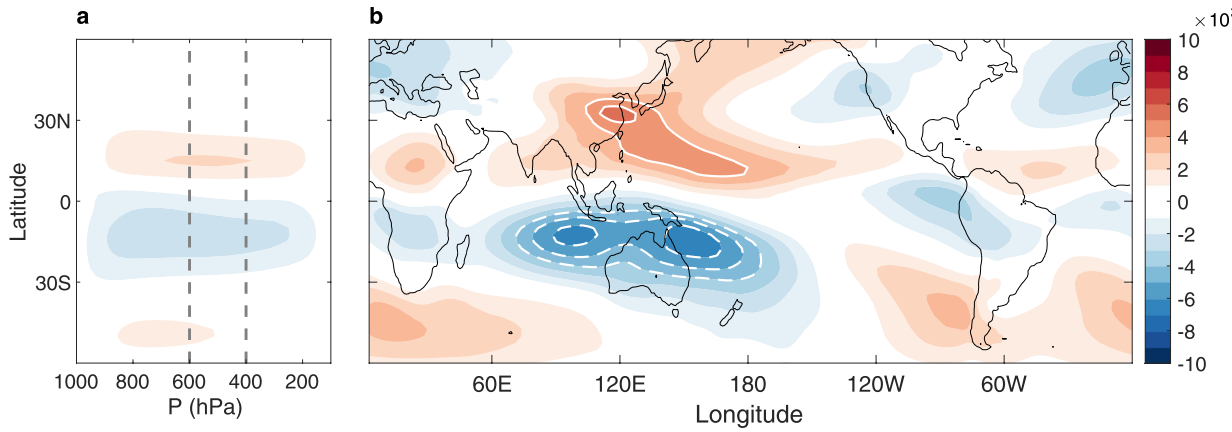

Figure 1. The climatological meridional circulation. (a) The zonally averaged circulation (Hadley cells) as function of latitude and pressure with the dashed lines denoting the 400 hPa and 600 hPa. (b) The annual average of the meridional longitudinally dependent circulation, averaged between 400 hPa and 600 hPa, as function of longitude and latitude. Contour interval is 1×10^3 kg s^{-1} m^{-1}. White solid and dashed lines indicate absolute values larger than 4×10^3 kg s^{-1} m^{-1}.

The mass-weighted global meridional circulation (Hartmann, 2016) is represented by a stream function calculated using the zonally averaged meridional velocity $\bar{v}$

$$\psi(\phi, p, t) = \frac{2\pi a \cos\phi}{g} \int_0^p \bar{v}(\phi, p', t) dp', \tag{1}$$

where a is Earth's radius, g is the gravitational acceleration, ϕ is latitude, and p is pressure. The time average of this circulation is shown in Figure 1a. The two classical Hadley cells can be seen roughly between the equator and latitudes $\pm 30°$. However, the circulation, as defined by Equation 1, cannot account for any zonal asymmetry in the meridional circulation. The LMC can be calculated via the separation of the 3-D wind velocity field into a meridional component and a zonal one. Here we follow the notation of Hu et al. (2017). First, the divergence of the wind is calculated

$$D = \nabla \cdot \vec{V}, \tag{2}$$

where $\vec{V} = (u, v)$ is the full horizontal wind vector. Then, the velocity potential χ is calculated via

$$\nabla^2 \chi = D. \tag{3}$$

This equation can be solved either via decomposition into spherical harmonics, or by formulating the problem as a set of finite difference linear equations and inverting the Laplacian. The methods are equivalent and in this study the latter is used. The potential function is then used to calculate the divergent wind

$$\nabla \chi = \vec{V}_{\text{div}}, \tag{4}$$

where $\vec{V}_{\text{div}} = (u_{\text{div}}, v_{\text{div}})$. The zonal (meridional) component of the divergent wind is associated with closed east-west (north-south) oriented circulations, such as the Walker (Hadley) cell. Therefore, the divergent wind can be used, similar to Equation 1, to calculate the longitudinally dependent meridional circulation

$$\psi(\lambda, \phi, p, t) = \frac{1}{g} \int_0^p v_{\text{div}}(\lambda, \phi, p', t) dp', \tag{5}$$

where λ is longitude. Note that the integral of Equation 5 over longitude gives the classical zonally averaged meridional circulation (Equation 1). A simplified representation of the meridional circulation can be defined by averaging ψ between 600 and 400 hPa

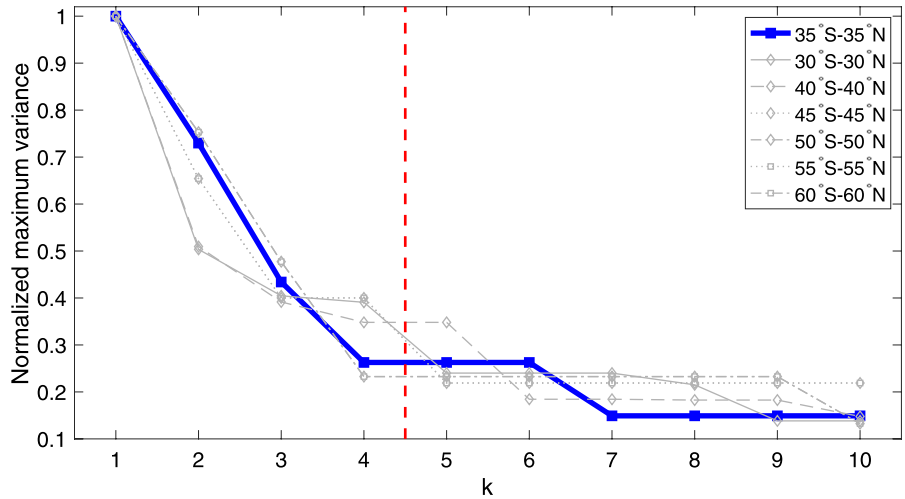

Figure 2. Normalized maximal cluster variance as function of the number of clusters used in the analysis. Shown is the analysis with data restricted to the latitudinal range of 35°S–35°N (blue), and the analysis for other latitudinal ranges. Dashed red line denotes the 4 clusters cutoff used in the analysis.

$$\tilde{\psi}(\lambda,\phi,t)=\frac{1}{\Delta p}\int_{p_1}^{p_2}\psi(\lambda,\phi,p',t)dp', \tag{6}$$

where $p_1=400$ hPa, $p_2=600$ hPa, and $\Delta p=p_2-p_1$. As discussed above, this is the region where the zonal mean meridional circulation reaches its maximum. We will use this simplified definition of the longitudinally dependent meridional circulation (denoted hereafter as LMC) throughout this study. The time averaged LMC is shown in Figure 1b. It has a very strong zonal dependence — it is most pronounced in the Indo-Pacific region, between 70 and –180°E, and is much stronger in the Southern hemisphere.

2.2. Interannual Variability Analysis Using Hierarchical Clustering

The temporal variability of the LMC can be explored using cluster analysis, in which spatial patterns that are prone to repeat in time are identified. Unlike methods based on principal components requiring that the different patterns are orthogonal to each other, clustering allows the identification of commonly occurring patterns that may not be orthogonal. There are several methods to perform cluster analysis; here, we use hierarchical clustering that was successfully applied to the studies of atmospheric dynamics (e.g., Cheng & Wallace, 1993; Horton et al., 2015; Kao & Yu, 2009; Totz et al., 2017). Other variants of the clustering method such as the *k*-means (e.g., Madonna et al., 2017) and self organizing maps (e.g., Feldstein & Lee, 2014) were used in climate studies. The data used here — the monthly mean longitudinally-dependent meridional circulation at each time step averaged over 400–600 hPa, is treated as an N dimensional vector where N is the number of grid points. Note that to isolate the interannual variability, we remove the seasonal cycle from the data (via the subtraction of the 12 monthly averages from the corresponding points of the monthly data). We analyze two data sets simultaneously, so that the number of samples is twice over the time span, thus increasing the robustness of the identified clusters. The method allows to find how the 960 vectors (2 data sets × 40 years × 12 months) are clustered in the N-dimensional space. Note that the analysis was repeated with different combinations of the data sets. Starting with the assumption that each point of the entire data set is a single cluster, the method then performs a hierarchical separation of the data to a decreasing number of clusters, combining previously identified clusters into new clusters using the Ward method of combining clusters based on minimal increase in cluster variance (Wilks, 2011). One then needs to decide what the optimal number of clusters is.

For the clustering analysis, we examine the meridional circulation in the latitudinal range of 35°S–35°N, where the LMC is most significant (Figure 1). Plotting the maximal cluster variance as function of the number of clusters, the optimal number of clusters can be identified (Figure 2, blue line). By definition, increasing the number

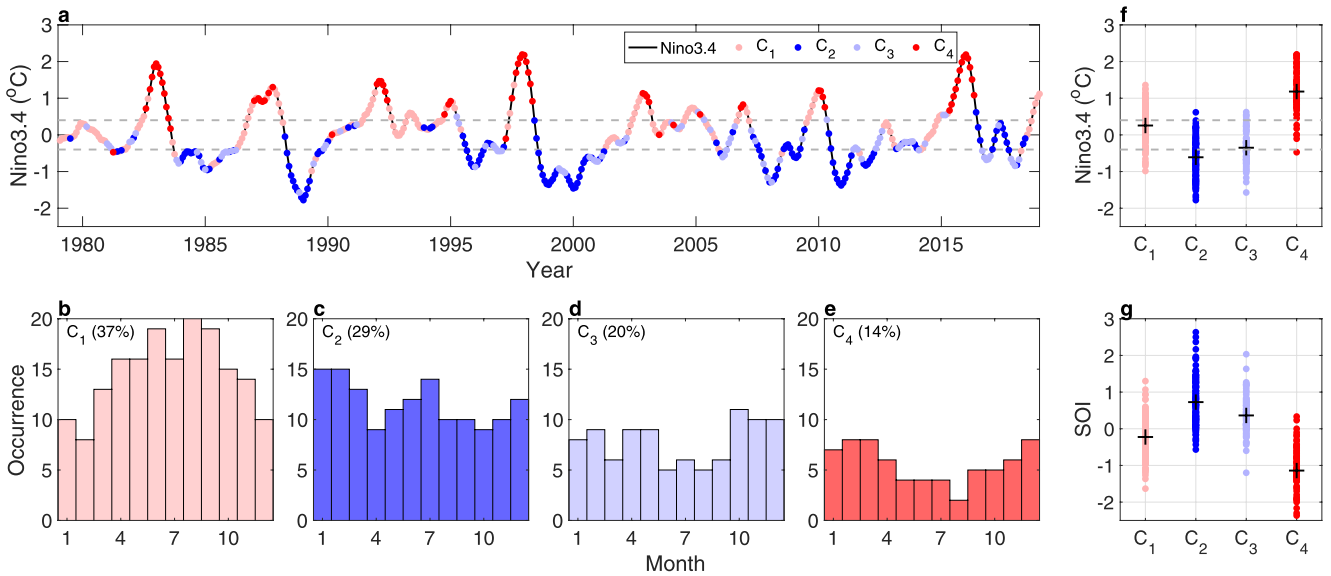

Figure 3. The time occurrence of the LMC interannual variability clusters. (a) The occurrence of each cluster plotted as colored dots on top of the El Niño-Southern Oscillation (ENSO) Nino3.4 index. (b)–(e) The occurrence of each cluster as function of the month of the year. Also shown is the total occurrence percentage of each cluster. (f) The occurrence of each cluster as function of the Nino3.4 index. (g) The occurrence of each cluster as function of the Southern Oscillation index. Horizontal dashed lines in (a) and (f) denote the ±0.4°C threshold used to define ENSO events.

of clusters results in a smaller variance (data vectors are better clumped together). However, the maximum cluster variance decreases substantially in the range of up to 4 clusters, while further increasing the number of clusters does not result in a significant reduction. Repeating the analysis for different latitudinal ranges results in a similar conclusion, strengthening the robustness of the analysis. Note that Kao and Yu (2009), who analyzed the interannual variability of the Pacific SST using hierarchical clustering, also found that 4 clusters best describe the variability of the SST. Finally, even though a given month from the two chosen data sets (ERA-Interim and NCEP, or ERA-Interim and ERA5) may be assigned to two different clusters, in practice each of the 4 clusters are found to contain predominantly the same months in each of the two data sets (only 8 of the 480 months are different for the first choice, none were different for the latter). Moreover, all the results discussed in this study are evident in all data sets, that is, the composites calculated for each cluster are similar, showing that the interannual variability of the LMC, as depicted by the clustering analysis, is robust over different data sets (see Figures S1–S3 in Supporting Information S1). In order to allow a direct comparison with previous studies (see above discussion), the results shown here are based on the ERA-Interim data, while the results for the two data sets are shown in the Supporting Information.

3. Results

We start by examining the occurrence of monthly data points that are assigned to each cluster, as function of time from 1979 to 2018, and as function of time during the year. Figure 3a shows the occurrence of the 4 clusters C_1, C_2, C_3, C_4 in different colors, marked over a time series of the Nino3.4 Index (SST anomalies averaged over 5°N–5°S, 120–170°W, with a 5-month running average). The Nino3.4 represents ENSO phenomenon, the leading mode of interannual variability in the tropics (e.g., Wang et al., 2017). ENSO events are typically defined when the Nino3.4 value exceeds ±0.4°C (gray dashed lines) for at least 6 consecutive months. We begin with a more qualitative examination of the relation between the clusters and El Niño/La Niña, and below analyze this more quantitatively. Points in the first cluster (marked by light red dots) seem to occur mostly during periods when the Nino3.4 is weakly positive and correspond to 37% of the analyzed months. The second cluster (blue) corresponds mostly to periods when the Nino3.4 is strongly negative (29% of months) and the third cluster (light blue) represents mostly periods when the Nino3.4 is weakly negative (20%). The fourth cluster (red) mostly represents periods when the Nino3.4 is strong positive (14%). Also shown is the month of the year of data vectors assigned to each cluster (Figures 3b–3e). Months assigned to cluster C_1 occur more frequently during the northern

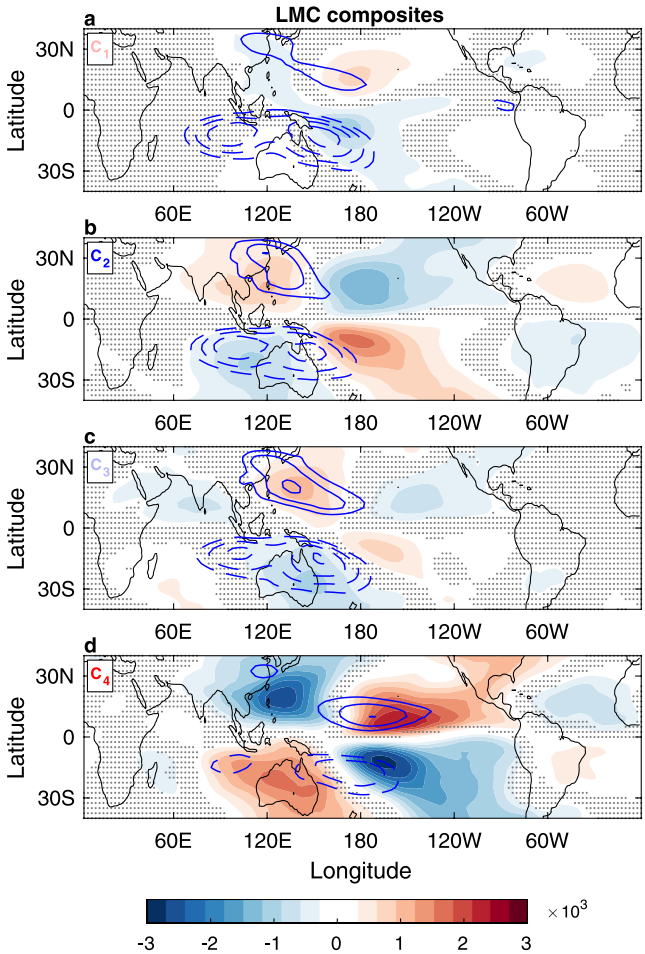

Figure 4. Composites of the anomalous LMC for each of the 4 clusters (shadings, in kg s^{-1} m^{-1}), and the full LMC composites for the months of each cluster (blue lines, with same values as a in Figure 1b). Dotted areas indicate regions where the cluster is not statistically significant.

hemisphere summer, while those in C_4 appear more during the northern hemisphere winter. On the other hand, months assigned to clusters C_2 and C_3 have only a weak dependence on the month of the year.

Previous work assumed the variability of the LMC to be dominated by ENSO and calculated it for different phases of the ENSO cycle based on the Nino3.4 Index (e.g., Nguyen et al., 2018), or the Southern Oscillation Index (SOI, e.g., Schwendike et al., 2014). Our methodology allows us to examine this hypothesis, as we calculate the LMC patterns using cluster analysis independently of the state of ENSO. Figures 3f–3g show the Nino3.4 and SOI indices, respectively, for all months of each LMC cluster. While our above discussion and Figure 3a suggest some relation between different clusters and the ENSO phases, the analysis in Figures 3f–3g show very clearly that there is no direct one-to-one correspondence between the two. Instead, there is a significant overlap in the Nino3.4 and SOI values for months corresponding to the different LMC patterns. Moreover, during some El Niño events cluster C_1 is present for a considerable part of the event duration, and in some events even more than C_4, for example, during the 1986–1987, 1991–1992, 2002–2003, and 2009–2010 events. However, the same cluster is also frequently present during periods with Nino3.4 weakly positive, and even during periods when Nino3.4 is negative. Similar arguments can be made for C_2 and C_3, both of which are present during periods when Nino3.4 is only weakly negative and during periods when it is strongly negative (La Niña events). We conclude that LMC patterns are not uniquely determined by the state of ENSO as quantified by these standard indices, a result that may not be very surprising given the diversity of ENSO spatial patterns and the inability of any scalar index to represent it. We will see below (Section 3.2) that there is still a relation between the LMC clusters and different flavors of ENSO as was hypothesized in previous work, even if it cannot be expressed in terms of these indices as was assumed previously.

3.1. Quantifying the Spatial Characteristics of Different LMC Patterns

Based on the classification of each of the 480 months in the data set, a composite of the LMC is calculated for each cluster from the ERA-Interim data set (Figure 4). Note that composites based on the NCEP and ERA5 reanalyzes give very similar spatial patterns, showing that the clusters are robust over different data sets (Figure S1 in Supporting Information S1). For each composite we calculate the 95% confidence level using a nonparametric two-sided statistical test, where the absolute value of the cluster at each grid point is verified to be larger than the one calculated with a random selection of months, 95% of the times. Marking the regions where the results are not statistically significant with gray dots, it is clear that the cluster structure is significant in all regions where the clusters have large values.

The anomalies represented by the clusters are all antisymmetric about the equator, an indication of a similar weakening or strengthening of the circulation in both the northern and southern hemisphere LMC. Below we discuss this aspect in relation to the SST analysis (Section 3.2.1). The clusters also show an east-west asymmetry, peaking around a longitude range between 90°E and 150°W. The pattern of two maxima and two minima indicates a shift of the LMC either eastward (C_1 and C_4) or westward (C_2 and C_3) relative to climatology. This zonal movement of the meridional circulation was indirectly observed in relation to ENSO (Feng et al., 2017; Guo & Tan, 2018), and could be viewed as part of the shifts in the Walker circulation during ENSO events (e.g., Tanaka et al., 2004), however its direct identification is made possible in our study due to the definition of the LMC. In addition, the patterns indicate that the LMC also shows variability in its latitudinal location, width and north-south skewness. In order to quantify these variations, we define the LMC most significant region as the region with values larger than 7×10^3 kg s^{-1} m^{-1}, and calculate the weighted average location, standard deviation, and skewness for each cluster

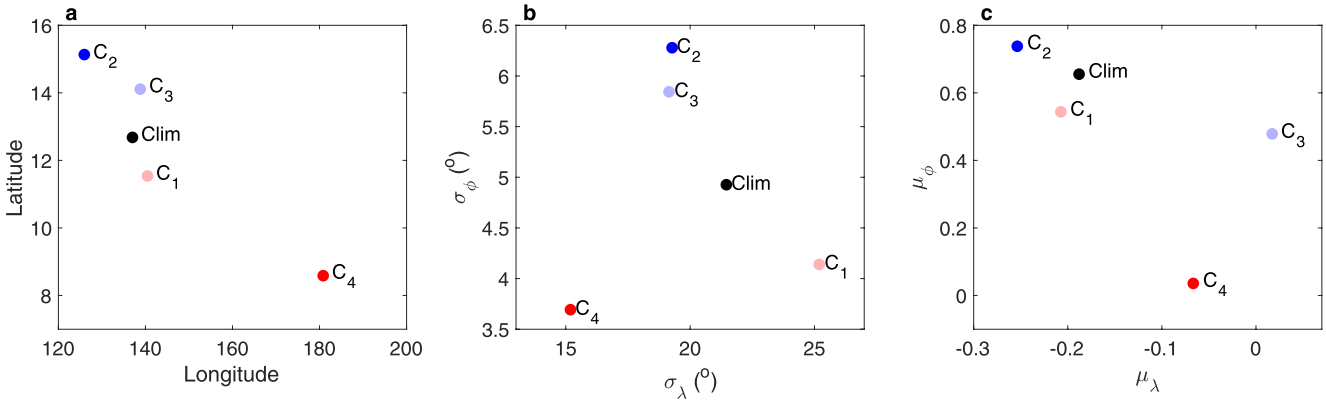

Figure 5. The spatial characteristics for each cluster and the DJF climatology. Shown are: (a) center of mass, (b) the standard deviation, and (c) the skewness. The colors denoting each cluster are the same used in Figure 3.

$$\left(\bar{\lambda}_i, \bar{\phi}_i\right) = \frac{\sum(\lambda,\phi)\tilde{\psi}_i}{\sum\tilde{\psi}_i},\quad (\sigma_{\lambda,i}, \sigma_{\phi,i}) = \frac{\sum\left(\left[\lambda-\bar{\lambda}_i\right]^2, \left[\phi-\bar{\phi}_i\right]^2\right)\tilde{\psi}_i}{\sum\tilde{\psi}_i},$$
$$(\mu_{\lambda,i}, \mu_{\phi,i}) = \frac{\sum\left(\left[\lambda-\bar{\lambda}_i\right]^3, \left[\phi-\bar{\phi}_i\right]^3\right)\tilde{\psi}_i}{\left(\sigma^3_{\lambda,i}, \sigma^3_{\phi,i}\right)\sum\tilde{\psi}_i}, \tag{7}$$

where $\left(\bar{\lambda}_i, \bar{\phi}_i\right)$, $(\sigma_{\lambda,i}, \sigma_{\phi,i})$, and $(\mu_{\lambda,i}, \mu_{\phi,i})$, are the longitude and latitude of the center, the standard deviation, and the skewness of the LMC cluster, respectively, and $\tilde{\psi}_i$ is the LMC averaged over the December-January-February (DJF) months of the ith cluster.

The shifts and skewness of the LMC are summarized in Figure 5. Most apparent is the eastward shift of the center locations during strong El Niño (C_4) (Figure 5a), with a longitudinal shift of around 50°. During the strong La Niña related months (cluster C_2), the LMC is shifted by about 15° to the west. In addition, there is an up to 4° north-south shift of the LMC center, where C_1 and C_4 are shifted to the south, and C_2 and C_3 to the north. The longitudinal extent of the LMC (Figure 5b) does not change much for the different clusters, but the latitudinal extent does exhibit a clear shift, where C_1 and C_4 are getting narrower, and C_2 and C_3 wider. Together with the shift of the mean location, this implies that the LMC is more equatorially confined during C_1 and C_4 than during C_2 and C_3. This finding is consistent with the behavior of the zonally averaged Hadley circulation during ENSO (Caballero, 2007; Oort & Yienger, 1996), but with our longitudinally depended analysis it is even more pronounced. Figure 5a shows negative correlation between the shifts in the zonal and meridional directions, while panel b shows that there is no obvious relation between the extent of the clusters in latitude and longitude. Looking at the change in the skewness (Figure 5c) we see that during C_4 the north-south asymmetry disappears. These morphological changes in the LMC indicate that the interannual variability of the large scale tropical circulation is not limited to strengthening and weakening, but also involves significant shifts. Next, we explore how these modifications are expressed in the full 3-D flow.

Since the LMC, as calculated and plotted above, captures only the meridional component of the tropical large-scale circulation, a better understanding of the changes on interannual time scales in the actual 3-D circulation can be achieved using a Lagrangian perspective, in which air parcels trajectories are followed given an initial position (Raiter et al., 2020). Note that a similar methodology was used by Feng et al. (2017) to study ENSO teleconnections. The full circulation, depicted by the Lagrangian analysis, is affected not only by the LMC but also by the zonal circulation and by the rotational (horizontal) circulation (e.g., Raiter et al., 2020). Based on the cluster analysis (Figure 4), we set two regions of initial positions around the equator, one between 90°E and 150°E, and another between 150°E and 150°W (Figure 6, black dots). These regions cover the main dipole signal in the 4 clusters. The air parcels initial positions are set at a height of 500 hPa, and are followed for 20 days forward and 20 days backward in time. This allows a sufficient coverage of the full tropical circulation (see Raiter et al. (2020) for a detailed discussion of the methodology). We examine the circulation during the averaged flow conditions

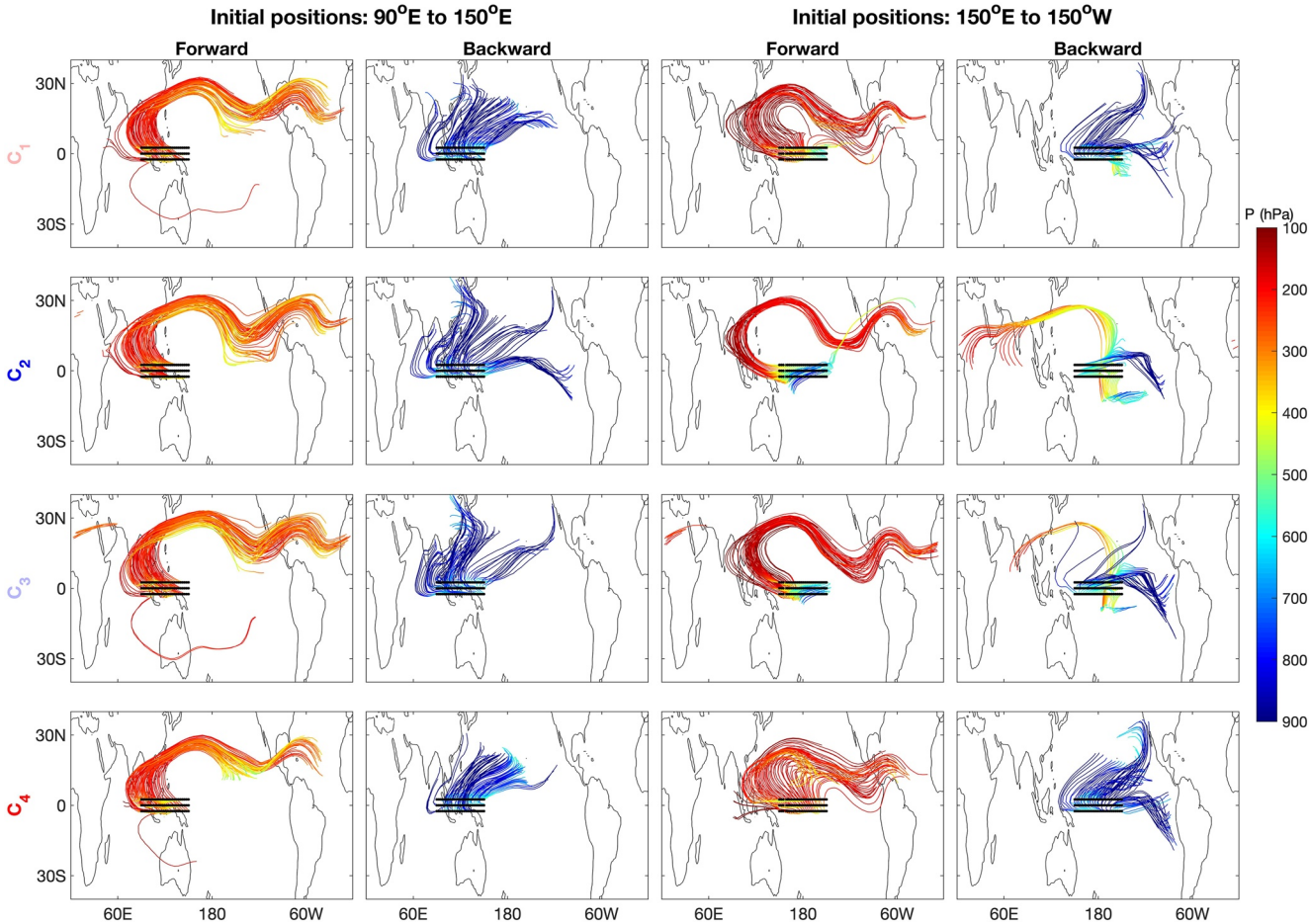

Figure 6. Trajectories of air parcels during DJF months associated with each cluster. Initial positions are set around the equator in two main regions: 90°E to 150°E, and 150°E to 150°W. The air parcels are initiated from a height of 500 hPa and followed for 20 days forward, and 20 days backward. The color indicates the height (hPa) of the parcel during its trajectory.

in the months associated with each cluster. Since the tropical circulation has a significant seasonal cycle, we define the states using only the DJF months, but a similar behavior (in the opposite hemisphere) is apparent when looking at the June-July-August months. Note also that the characteristics of the trajectories in all 4 clusters and for the two regions or initial position were found to be similar in all three data sets. In the Supporting Information (Figures S2 and S3 in Supporting Information S1) we show the analysis for all data sets.

We start with a general description of the LMC that is common to all clusters during DJF. The air, rising over the maritime continent, moves westward with the trade winds, then northward with the LMC, and then enters the jet streams moving eastward. Part of the circulation descends in the mid-Pacific and part descends over the Americas (Raiter et al., 2020). The backward trajectories show how the air is converging to the equatorial region from the lower altitude central and eastern Pacific, mostly from the northern hemisphere.

The interannual variability is apparent in the different trajectories driven by the circulation associated with each of the clusters. First, we look at the most distinct clusters, C_2 (La Niña related) and C_4 (El Niño related). During months corresponding to C_4, the western region (left panels) exhibits a weaker and more confined circulation, than during C_2; this is expected, given that the circulation moves eastward during El Niño events. Conversely, in the eastern region (right panels), a much more pronounced meridional circulation is observed during C_4. During C_2 months, the air parcels either stay in place or move to the Western Pacific before going north, consistent with the circulation moving west during La Niña events, while during C_4 conditions, air parcels move directly upward and to the north. In addition, during C_2 conditions, the air parcels originating in the western region are affected by a much stronger and larger-scale circulation than in the climatology. The east-west shift between C_2 and C_4 is

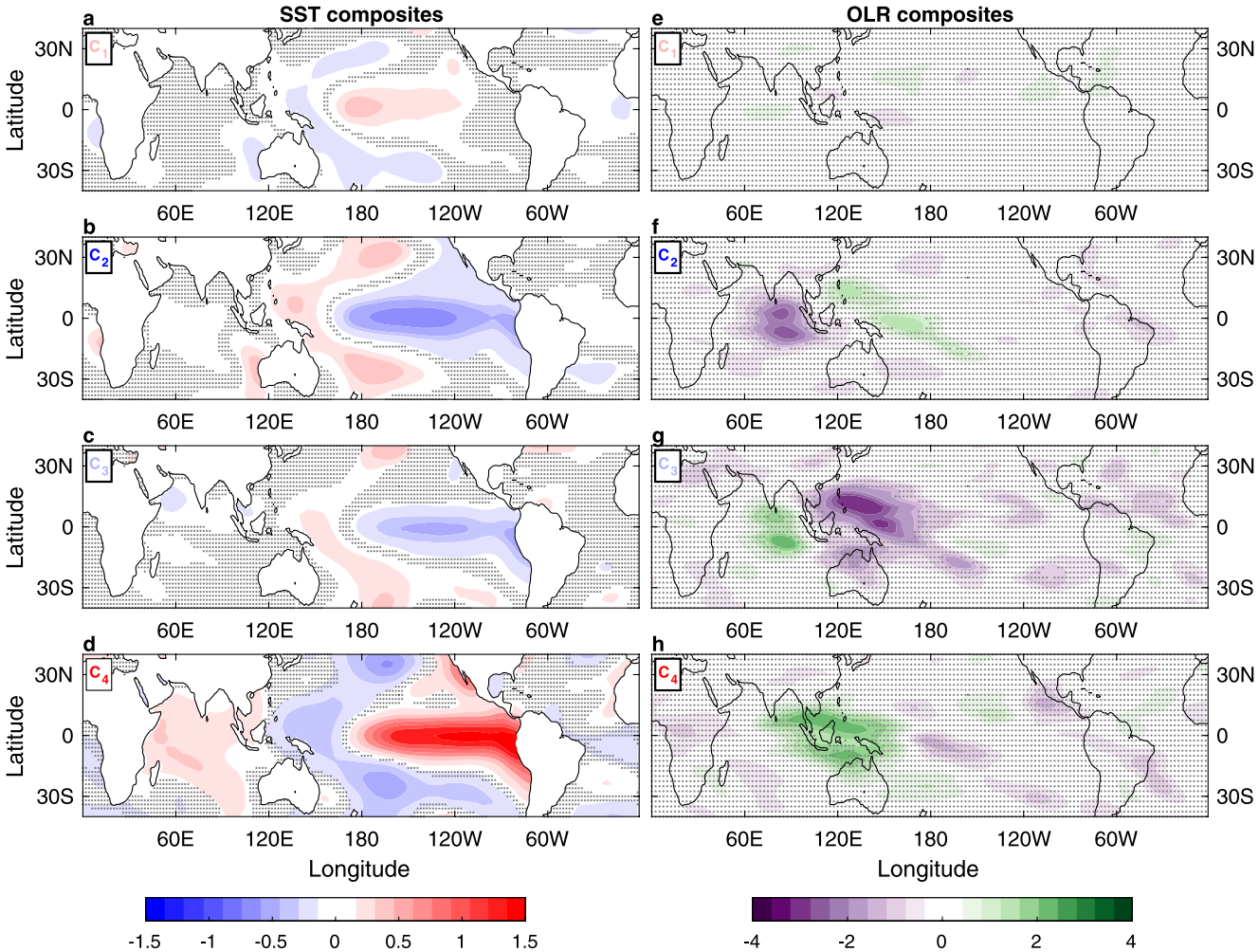

Figure 7. (a–d) Composites of Sea Surface Temperature anomalies for each of the clusters (in °C). (e–h) Composites of 10–90 days bandpass outgoing long-wave radiation (W m^{-2}). Regions below the 95% confidence level are marked with gray dots.

also apparent in the back trajectories on the second and fourth columns of Figure 6. These features of the full 3-D trajectories are consistent with the analysis of the LMC in Figure 5, also showing significant shifts in the east-west and north-south directions, as well as changes in the latitudinal extent of the circulation.

Further details on the complexity of the relation between the LMC variability and ENSO are revealed by clusters C_1 and C_3. For example, during C_3, air parcels originating from the eastern initial positions (Figure 6, third column) move farther to the east than all other clusters. After 20 days, these parcels reach the Middle East, while in the other clusters they only reach Western Europe. Thus C_3 is not merely a weak version of C_2, although both are associated with periods when Nino3.4 is negative. Similarly, some of the parcels originating from the western region (Figure 6, first column) during C_1 reach further to the west than during C_3, even though the former is associated with periods when the Nino3.4 is positive and the latter when it is negative.

3.2. Drivers and Teleconnections of LMC Variability

3.2.1. Drivers of the LMC Variability

The classification of the temporal variations of the LMC into the 4 clusters can be used to search for accompanying variability in other oceanic and atmospheric variables that might act as drivers for the LMC. We now calculate SST composites for each LMC cluster (seasonal cycle removed similarly to the LMC, Figures 7a–7d). The ENSO signal is clearly identified in the strong SST anomalies at the central to east equatorial Pacific, with C_2 and C_3

Table 1
The Dependence of the LMC on the SST and MJO (Equation A1), and the Dependence of Air Temperature and Precipitation on the LMC and SST (Equations 10 and 11), for the 4 Clusters

	LMC			Air Temperature			Precipitation		
	SST(β_L)	MJO(γ_L)	R^2	LMC(β_T)	SST(γ_T)	R^2	LMC(β_P)	SST(γ_P)	R^2
C_1	0.80	0.09	0.64	0.21	0.39	0.33	0.81	0.09	0.78
C_2	0.82	0.24	0.74	0.15	0.77	0.82	0.89	0.06	0.88
C_3	0.76	0.27	0.65	0.16	0.73	0.75	0.87	0.06	0.85
C_4	0.84	0.25	0.77	0.04	0.84	0.77	0.73	0.25	0.90

Note. Shown are the multi-linear regression coefficients, and the R2 for each case.

associated with a La Niña phases and C_1 and C_4 with an El Niño phases. The 4 SST patterns are overall symmetric around the equator, mostly in the Central Pacific region, which is a characteristic of ENSO. If the LMC-SST relation is indeed strong (as we will demonstrate below), this explains why the LMC patterns (Figure 4) also exhibit symmetry around the equator.

The two pairs of clusters reveal the action on the LMC by the different ENSO flavors (Capotondi et al., 2015; Kao & Yu, 2009). In the positive SST-related clusters, C_4 relates to a more classical eastern Pacific (EP) El Niño (e.g., Rasmusson & Carpenter, 1982), while C_1 relates to a central Pacific (CP) El Niño, also referred to as El Niño Modoki (Ashok et al., 2007). In the negative SST-related clusters, C_2 relates more to CP La Niña, and C_3 relates more to EP La Niña. These relations are also apparent in the temporal variations of the LMC clusters (Figure 3a), similar to those found for the SST variability (Figure 1; Capotondi et al., 2015): The 2004–2005 (1997–1998) El Niño event is characterized mostly by C_1 (C_4) LMC clusters, and the 1988–1989 (2007–2008) La Niña event is characterized mostly by C_2 (C_3). Furthermore, the SST pattens associated with the LMC (Figures 7a–7d) bear some resemblance to the 4 SST patterns found by Kao and Yu (2009) to best describe the Eastern and Central Pacific ENSO events, strengthening the role of the spatially dependent SST interannual variability in setting the LMC.

We would like next to determine to what degree can a given driver, such as the SST, be related to the LMC variability using regression analysis between the time series representing the variability in the driver and in the LMC. For this purpose, the LMC is projected on each of its cluster averages $C_i(\lambda, \phi)$ shown in Figure 4,

$$\tilde{\psi}_i(t) = \frac{1}{2\pi\Delta\phi} \int_{\phi=-\frac{\pi}{3}}^{\frac{\pi}{3}} \int_{\lambda=0}^{2\pi} \tilde{\psi}(\lambda, \phi, t) C_i(\lambda, \phi) \cos\phi d\lambda d\phi, \tag{8}$$

and the resulting time series are then normalized by their standard deviation. Similarly, all other fields are projected onto their respective cluster-average composites and normalized.

The dependence of the LMC on the SST is now revealed by calculating the regression,

$$LMC(t) = \alpha_L + \beta_L SST(t). \tag{9}$$

The fraction of variance explained by the SST for C_2, C_3, and C_4 is around 68%, 58%, and 71%, respectively.

While the above analysis (as well as previous studies, e.g., Schwendike et al., 2014) indicates that LMC variability is closely related to SST anomalies, it might also be influenced by other atmospheric phenomena (Schwendike et al., 2021). Given that the MJO (Madden & Julian, 1971; Zhang, 2005) is the largest intraseasonal signal in the tropics, we attempt to find connections to this signal as well, with detailed analysis in Appendix A, briefly summarized here. The MJO-related OLR composites for each cluster are shown in Figures 7e–7h. The structure of the composites resembles different phases of the MJO (Wheeler & Hendon, 2004): C_2 is similar to MJO phase 6, C_3 is similar to phases 2 and 3, and C_4 is similar to phase 5. Note that the composites of the two La Niña related clusters (C_2 and C_3, Figures 7b and 7c) correspond to opposite phases of the MJO (Figures 7f and 7g), supporting the MJO being a separate driver from the ENSO-related SST. A multivariate regression analysis of the LMC as function

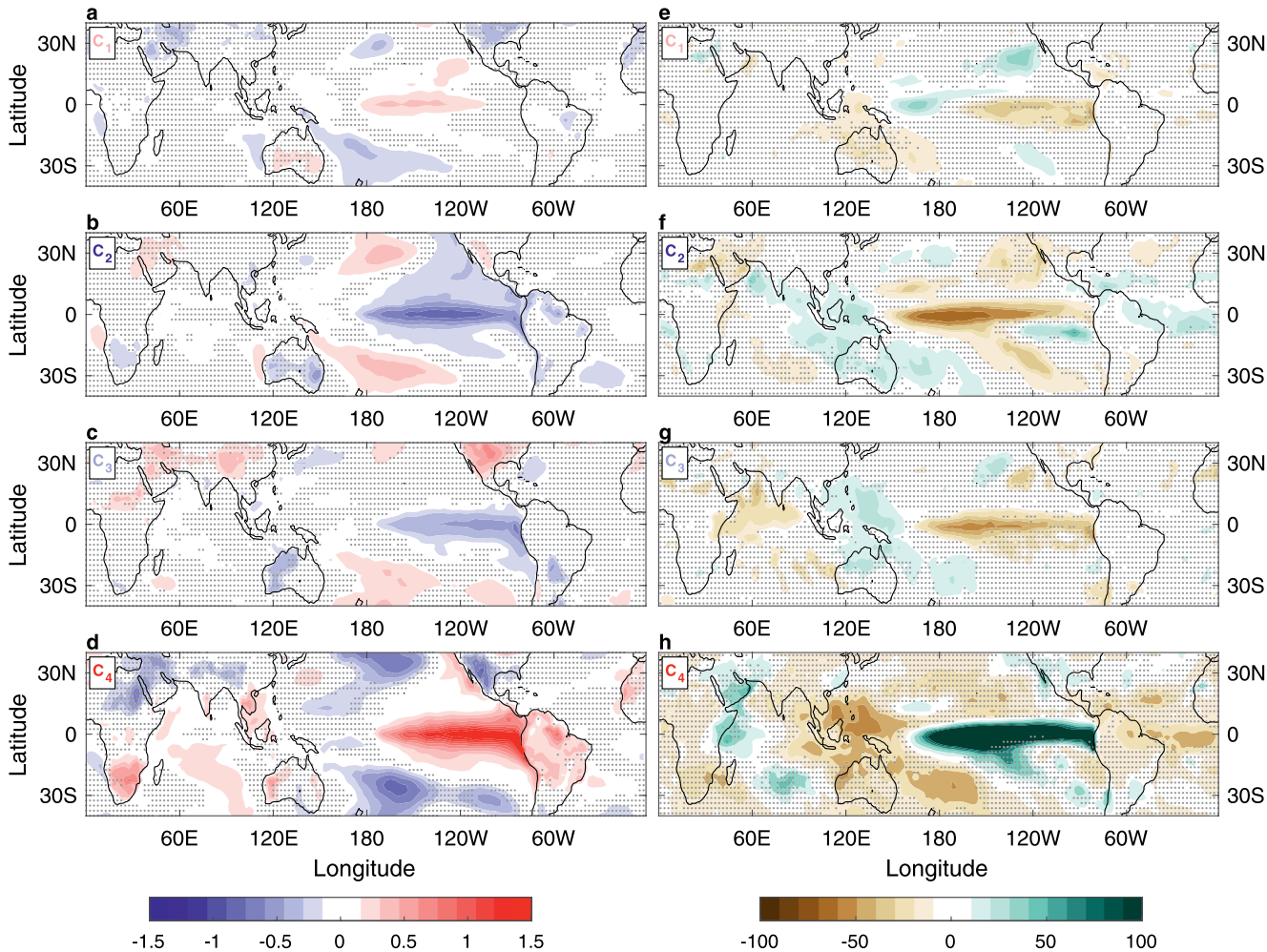

Figure 8. Same as in Figure 4 but (a–d) for the 2 m air temperature (in °C), and (e–h) for the fractional precipitation change (in percentage).

of both the normalized SST and normalized MJO (Table 1 and Appendix A) shows that the MJO explains some 6%–7% of the LMC variance for clusters $C_{2,3,4}$, indicating that the MJO effects are weak yet nonnegligible, consistent with the findings of, for example, Seo et al. (2016); Schwendike et al. (2021).

3.2.2. Teleconnections Involving LMC Variability

Next, we relate the variability of the LMC to the variability of air temperature at 2 m and of the total precipitation, both fields of obvious socioeconomic relevance. The two fields are expected to be influenced by the magnitude and patterns of the LMC, or at least be closely related to these patterns. A stronger LMC implies more upward motion in the tropics and therefore stronger precipitation. At the same time, of course, latent heat release due to this precipitation may drive atmospheric motions related to the LMC. Similarly, surface air temperature over the equatorial Pacific is expected to be closely coupled with the SST and therefore be a driver, yet remote signals are more likely to be consequences of the LMC variability and of the ENSO variability that drives it. It is therefore difficult to clearly identify consequences versus drivers here, but the relation to these fields is clearly interesting and important and this issue is further discussed below.

The composites for the surface air temperature and precipitation are shown in Figure 8, and are statistically significant where the amplitude is substantial, indicating that the interannual variability of both air temperature and precipitation is strongly correlated with the LMC variability. There are major differences between the fields: the precipitation variability (Figures 8e–8h) is mostly confined to the equatorial Pacific region (Figures 4a–4d); the variability in the air temperature (Figures 8a–8d) is seen over much broader regions, reaching higher latitudes, Africa and the Middle East. Noting the above discussion of drivers versus consequences, one would expect re-

mote surface air temperature signals, such as those seen over South Africa, North America, the Middle East etc., to likely be an effect of the LMC patterns or of the ENSO states that force the LMC variability, rather than be a driver. As mentioned above, surface air temperature over the ENSO region is likely influenced by the SST and may be expected to act as a driver of LMC variability.

For each cluster, we calculate the multiple linear regression between the temperature or precipitation and the LMC and SST,

$$AirT(t) = \alpha_T + \beta_T LMC(t) + \gamma_T SST(t) \tag{10}$$

and

$$P(t) = \alpha_P + \beta_P LMC(t) + \gamma_P SST(t), \tag{11}$$

respectively. The results for the coefficients β_T, γ_T, β_P and γ_P are shown in Table 1. For all cases, the linear regression captures most of the signal (R^2 under air temperature and precipitation columns mostly above 0.75). Although the LMC and SST are correlated (not independent), more of the variance of the precipitation variability is explained by the LMC variability than by the SST variability (as also seen by the fact that $\beta_P \gg \gamma_P$, remembering that all time series used are normalized). We note, though, that the LMC and the precipitation fields vary on shorter time scales than the SST, which may account for the tighter correlation. Therefore, the mechanism governing the precipitation variability, while being mostly a result of the ENSO condition, is likely mediated by the LMC variability. The dependence of the air temperature on the LMC and SST is less clear, but overall it can be seen that the air temperature is better correlated with the SST. This is not surprising as one expects the 2 m air temperature to be tightly coupled with the SST, although there are areas over land where the air temperature is more free to change, not being coupled to the local SST.

The interaction between the LMC and temperature and precipitation fields is by no means one-way. Because the meridional circulation is driven by meridional temperature gradient, changes of temperature in the midlatitudes, without any changes in the equator, will induce changes in meridional temperature gradient, which, in turn, may affect the meridional circulation. Similarly, if the LMC weakens, convection in the rising branch weakens, which reduces rainfall and may increase surface shortwave radiation, hence surface temperature. These examples further demonstrate that this is a complex and noisy system with many possible participating factors.

4. Summary

The large scale meridional circulation is a key element of the climate system, responsible for the energy and moisture transport from the equatorial region to the subtropics. While traditionally defined as the zonally averaged meridional circulation in the tropical region (Hadley circulation), in recent years, several studies examined the longitudinal dependence of the meridional circulation via decomposition of the three-dimensional atmospheric flow into LMC, local zonal circulation, and rotational flow, using a Helmholtz decomposition into divergent and rotational flows (Keyser et al., 1989). This enables the examination of the meridional circulation at each longitude separately (e.g., Nguyen et al., 2018; Raiter et al., 2020; Schwendike et al., 2014; Schwendike et al., 2015). These studies provided a useful analysis of the regionality and variability of the local meridional circulation, focusing on its climatology (e.g., Raiter et al., 2020), its ENSO related variability (e.g., Nguyen et al., 2018; Schwendike et al., 2014; Staten et al., 2019), and on its response to observed climate change (e.g., Schwendike et al., 2015; Staten et al., 2019).

In this study we investigate the interannual variability of the LMC using hierarchical clustering, and a Lagrangian perspective that allows the identification of the actual large-scale circulation in the tropics. We use cluster analysis that allows us to identify the main spatial patterns of variability of the LMC, independently of the SST variability. We then examine the relation to ENSO, the MJO, and related large-scale air temperature and precipitation variability. We find that the interannual variability can be represented by 4 clusters, and this allows us to characterize the morphology of the LMC as expressed in its zonal and meridional shifts and expansion/contraction. Specifically, we find that most apparent is the eastward shift of the center locations during strong El Niño, and westward shift during strong La Niña-related months. We also find that during El Niño-related months, the LMC is more confined to the equatorial region, while the opposite happens during La Niña-related months, consistent with previous studies (Caballero, 2007; Oort & Yienger, 1996). These studies examined the zonal-mean

Hadley circulation, and it is possible that the understanding of the local response of the LMC to ENSO-related SST will contribute to an improved understanding of the response of the zonal mean as well. We supplement this morphological analysis with a calculation of Lagrangian air trajectories, showing the full changes in the interannual tropical circulation. We find that the east-west movement of the circulation is indeed the main variability on interannual time scales, and that the LMC is dominant in setting the 3-D circulation and its variability.

Using the cluster analysis we then examine the SST patterns corresponding to each LMC variability mode as represented by the averaged SST over months belonging to each of the LMC clusters. We find that while there is no one-to-one correspondence between the NINO3.4 or SOI ENSO indices and the LMC variability modes, the SST composites for different LMC patterns do relate to the different ENSO flavors (East and Central Pacific). The LMC is therefore affected by the variety of ENSO states (Capotondi et al., 2015; Kao & Yu, 2009). We find using regression analysis that the appropriate SST patterns calculated via the cluster analysis can explain a large fraction (63%–71%) of the LMC temporal variance. We also find that a rather small part of the LMC variance (6%–8%) is explained by MJO-related variability (consistently with Schwendike et al., 2021). Further clustering-based analysis of the large-scale global response of precipitation and surface air temperature reveals teleconnections to remote locations such as South Africa, the Middle East and North America that are likely related to the ENSO driving of the LMC.

To conclude, we find complex shifts and morphological changes of the longitudinally dependent meridional circulation as part of its interannual variability, driven mostly be SST patterns. The clustering analysis which we use to examine the LMC and its relation to the SST allows to quantify the effect on the LMC of standard ENSO indices versus different flavors of El Niño and La Niña. The detailed dynamical atmospheric mechanisms behind these findings, such as how the different drivers set the different LMC spatial patterns, are not completely clear and require further study. It seems that similar clustering analysis of projected future changes to the LMC may bring interesting insights.

Appendix A: Role of the MJO in Affecting LMC Variability

To examine the possible connection of the LMC clusters to the Madden-Julian Oscillation (MJO), we choose here to represent the MJO state using the daily outgoing long-wave radiation (OLR), bandpass filtered between 30–96 days, and zonal wavenumber 1–5 (Wheeler & Kiladis, 19s99). We take the monthly averages of the daily data and calculate the MJO-related OLR composites for each cluster (Figures 7e–7h). We again calculate the nonparametric 95% significance level for all longitudes. While the typical amplitude of the MJO composites is an order of magnitude smaller than that of the monthly climatology of the OLR field, OLR composites for clusters 2–4 include regions in which the composite value is statistically significant, and more importantly, the structure of the signals resembles different phases of the MJO (Wheeler & Hendon, 2004): C_2 is similar to MJO phase 6, C_3 is similar to MJO phases 2 and 3, and C_4 is similar to MJO phase 5. Note that the two La Niña related clusters (C_2 and C_3) are related to opposite phases of the MJO.

The dependence of the LMC on the SST and MJO can be revealed by calculating the multivariate regression,

$$LMC(t) = \alpha_L + \beta_L SST(t) + \gamma_L MJO(t). \tag{A1}$$

The results are shown in Table 1 (first 3 columns). Aside from C_1, all the apparently El Niño-Southern Oscillation (ENSO) related clusters are better explained when the MJO is included in the regression. Together, the SST and the MJO time series explain between 64% and 77% of the LMC time series variance. As can be seen by the regression coefficients, the MJO contributes significantly except for C_1. When performing the regression with the MJO alone, some 6%–7% of the LMC variance is explained for clusters $C_{2,3,4}$, emphasizing the role of the MJO in setting the LMC patterns. This dependency might be complicated due to the interplay between the MJO and ENSO (e.g., Hendon et al., 2007; Liu et al., 2021; Tang & Yu, 2008). For instance, May MJO in the western Pacific leads El Niño conditions in the subsequent December (e.g., Hendon et al., 2007), while ENSO in turn impacts the MJO over the Maritime continent by shifting it south of the equator during eastern Pacific El Niño winters (Liu et al., 2021). To examine this ENSO-MJO-LMC interaction, we first remove the ENSO signal from the LMC. This is done by calculating the regression of the SST and the LMC, and then subtracting the LMC reconstructed from this regression from the full LMC time series for each cluster. This gives LMC time series that are completely independent of the SST variability. This residual, explaining 32%, 42%, and 29% of the LMC

variance, can be regressed with the MJO-related OLR revealing the independent effect of the MJO on the LMC. We find that for clusters C_2, C_3, and C_4, the MJO explains 19%, 17%, and 21% of the residual LMC signal, respectively. Therefore, we find that the MJO is correlated with the LMC independently from the SST variability. Finally, the overall LMC relation to the MJO, while somewhat marginal, is consistent with the findings of several other studies (e.g., Schwendike et al., 2021; Seo et al., 2016) that analyzed the effects of different phases of the MJO on the amplitude of the LMC.

Data Availability Statement

Data is available via the Harvard Dataverse: https://doi.org/10.7910/DVN/KTBSCZ.

Acknowledgments
This research has been supported by the Israeli Science Foundation (Grant 996/20), the Weizmann Institute Helen Kimmel Center for Planetary Science, and the European Union's Horizon 2020 research and innovation programme under Grant Agreement 820829 (CONSTRAIN project). ET is supported by the NSF Climate and Large-Scale Dynamics program (AGS-1826 635), and thanks the Weizmann Institute for its hospitality during parts of this work.

References

Ashok, K., Behera, S. K., Rao, S. A., Weng, H., & Yamagata, T. (2007). El Niño Modoki and its possible teleconnection. *Journal of Geophysical Research*, *112*, C11007. https://doi.org/10.1029/2006JC003798

Caballero, R. (2007). Role of eddies in the interannual variability of Hadley cell strength. *Geophysical Research Letters*, *34*, 22705. https://doi.org/10.1029/2007GL030971

Capotondi, A., Wittenberg, A. T., Newman, M., Di Lorenzo, E., Yu, J.-Y., Braconnot, P., et al. (2015). Understanding ENSO diversity. *Bulletin of the American Meteorological Society*, *96*(6), 921–938. https://doi.org/10.1175/BAMS-D-13-00117.1

Chemke, R., & Polvani, L. M. (2019). Exploiting the abrupt $4 \times CO_2$ scenario to elucidate tropical expansion mechanisms. *Journal of Climate*, *32*(3), 859–875. https://doi.org/10.1175/JCLI-D-18-0330.1

Cheng, X., & Wallace, J. M. (1993). Cluster analysis of the northern hemisphere wintertime 500-hPa height field: Spatial patterns. *Journal of the Atmospheric Sciences*, *50*(16), 2674–2696. https://doi.org/10.1175/1520-0469(1993)050<2674:caotnh>2.0.co;2

Dee, D., Uppala, S., Simmons, A., Berrisford, P., & Poli, P. (2013). The ERA-interim reanalysis: Configuration and performance of the data assimilation system. *Quarterly Journal of the Royal Meteorological Society*, *137*(656), 553–597. https://doi.org/10.1002/qj.828

Feldstein, S. B., & Lee, S. (2014). Intraseasonal and interdecadal jet shifts in the northern hemisphere: The role of warm pool tropical convection and sea ice. *Journal of Climate*, *27*(17), 6497–6518. https://doi.org/10.1175/JCLI-D-14-00057.1

Feng, J., Chen, W., & Li, Y. (2017). Asymmetry of the winter extra-tropical teleconnections in the northern hemisphere associated with two types of ENSO. *Climate Dynamics*, *48*(7–8), 2135–2151. https://doi.org/10.1007/s00382-016-3196-2

Grise, K. M., Davis, S. M., Simpson, I. R., Waugh, D. W., Fu, Q., Allen, R. J., & Staten, P. W. (2019). Recent tropical expansion: Natural variability or forced response? *Journal of Climate*, *32*(5), 1551–1571. https://doi.org/10.1175/JCLI-D-18-0444.1

Guo, Y.-P., & Tan, Z.-M. (2018). Relationship between El Niño-southern oscillation and the symmetry of the Hadley Circulation: Role of the sea surface temperature annual cycle. *Journal of Climate*, *31*(13), 5319–5332. https://doi.org/10.1175/JCLI-D-17-0788.1

Hartmann, D. L. (1994). *Global physical climatology*. Academic Press.

Hartmann, D. L. (2016). Chapter 6 - Atmospheric general circulation and climate. In *Global physical climatology* (2nd ed., pp. 159–193). Elsevier. https://doi.org/10.1016/b978-0-12-328531-7.00006-2

Held, I. M., & Soden, B. J. (2006). Robust responses of the hydrological cycle to global warming. *Journal of Climate*, *19*, 5686–5699. https://doi.org/10.1175/JCLI3990.1

Hendon, H. H., Wheeler, M. C., & Zhang, C. (2007). Seasonal dependence of the MJO ENSO relationship. *Journal of Climate*, *20*(3), 531. https://doi.org/10.1175/JCLI4003.1

Hersbach, H., Bell, B., Berrisford, P., Hirahara, S., Horányi, A., Muñoz-Sabater, J., & Thépaut, J.-N. (2020). The ERA5 global reanalysis. *Quarterly Journal of the Royal Meteorological Society*, *146*(730), 1999–2049. https://doi.org/10.1002/qj.3803

Horton, D. E., Johnson, N. C., Singh, D., Swain, D. L., Rajaratnam, B., & Diffenbaugh, N. S. (2015). Contribution of changes in atmospheric circulation patterns to extreme temperature trends. *Nature*, *522*(7557), 465–469. https://doi.org/10.1038/nature14550

Hu, S., Cheng, J., & Chou, J. (2017). Novel three-pattern decomposition of global atmospheric circulation: Generalization of traditional two-dimensional decomposition. *Climate Dynamics*, *49*(9–10), 3573–3586. https://doi.org/10.1007/s00382-017-3530-3

Kanamitsu, M., Ebisuzaki, W., Woollen, J., Yang, S.-K., Hnilo, J. J., Fiorino, M., & Potter, G. L. (2002). NCEP-DOE AMIP-II reanalysis (R-2). *Bulletin of the American Meteorological Society*, *83*(11), 1631–1643. https://doi.org/10.1175/BAMS-83-11-1631

Kao, H.-Y., & Yu, J.-Y. (2009). Contrasting eastern-Pacific and central-Pacific types of ENSO. *Journal of Climate*, *22*(3), 615. https://doi.org/10.1175/2008JCLI2309.1

Karnauskas, K. B., & Ummenhofer, C. C. (2014). On the dynamics of the Hadley Circulation and subtropical drying. *Climate Dynamics*, *42*(9), 2259–2269. https://doi.org/10.1007/s00382-014-2129-1

Keyser, D., Schmidt, B. D., & Duffy, D. G. (1989). A technique for representing three-dimensional vertical circulations in baroclinic disturbances. *Monthly Weather Review*, *117*(11), 2463–2494. https://doi.org/10.1175/1520-0493(1989)117<2463:atfrtd>2.0.co;2

Liu, H., Feng, X., Tao, A., & Zhang, W. (2021). Intraseasonal variability of sea level in the western North Pacific. *Journal of Geophysical Research: Oceans*, *126*(6), e17237. https://doi.org/10.1029/2021JC017237

Madden, R., & Julian, P. (1971). Detection of a 40-50 day oscillation in the zonal wind in the tropical Pacific. *Journal of the Atmospheric Sciences*, *28*(5), 702–708. https://doi.org/10.1175/1520-0469(1971)028<0702:doadoi>2.0.co;2

Madonna, E., Li, C., Grams, C., & Woollings, T. (2017). The link between eddy-driven jet variability and weather regimes in the north Atlantic-European sector. *Quarterly Journal of the Royal Meteorological Society*, *143*(708), 2960–2972. https://doi.org/10.1002/qj.3155

Nguyen, H., Hendon, H. H., Lim, E. P., Boschat, G., Maloney, E., & Timbal, B. (2018). Variability of the extent of the Hadley circulation in the southern hemisphere: A regional perspective. *Climate Dynamics*, *50*(1), 129–142. https://doi.org/10.1007/s00382-017-3592-2

Oort, A. H., & Yienger, J. J. (1996). Observed interannual variability in the Hadley circulation and its connection to ENSO. *Journal of Climate*, *9*(11), 2751–2767. https://doi.org/10.1175/1520-0442(1996)009<2751:oivith>2.0.co;2

Raiter, D., Galanti, E., & Kaspi, Y. (2020). The tropical atmospheric conveyor belt: A coupled Eulerian-Lagrangian analysis of the large-scale tropical circulation. *Geophysical Research Letters*, *47*(10), e86437. https://doi.org/10.1029/2019GL086437

Rasmusson, E. M., & Carpenter, T. H. (1982). Variations in tropical sea surface temperature and surface wind fields associated with the southern oscillation/El Niño. *Monthly Weather Review*, *110*(5), 354. https://doi.org/10.1175/1520-0493(1982)110<0354:vitsst>2.0.co;2

Schwendike, J., Berry, G. J., Fodor, K., & Reeder, M. J. (2021). On the relationship between the Madden-Julian oscillation and the Hadley and Walker circulations. *Journal of Geophysical Research: Atmospheres*, *126*(4), e2019JD032117. https://doi.org/10.1029/2019JD032117

Schwendike, J., Berry, G. J., Reeder, M. J., Jakob, C., Govekar, P., & Wardle, R. (2015). Trends in the local Hadley and local Walker circulations. *Journal of Geophysical Research: Atmospheres*, *120*(15), 7599–7618. https://doi.org/10.1002/2014JD022652

Schwendike, J., Govekar, P., Reeder, M. J., Wardle, R., Berry, G. J., & Jakob, C. (2014). Local partitioning of the overturning circulation in the tropics and the connection to the Hadley and Walker circulations. *Journal of Geophysical Research: Atmospheres*, *119*(3), 1322–1339. https://doi.org/10.1002/2013JD020742

Seo, K., Lee, H., & Frierson, D. (2016). Unraveling the teleconnection mechanisms that induce wintertime temperature anomalies over the northern hemisphere continents in response to the MJO. *Journal of the Atmospheric Sciences*, *73*(9), 3557–3571. https://doi.org/10.1175/JAS-D-16-0036.1

Simpson, I. R. (2018). Natural variability in the width of the tropics. *US CLIVAR Variations*, *16*(2), 14–20. https://doi.org/10.5065/D69Z93QF

Staten, P. W., Grise, K. M., Davis, S. M., Karnauskas, K., & Davis, N. (2019). Regional widening of tropical overturning: Forced change, natural variability, and recent trends. *Journal of Geophysical Research: Atmospheres*, *124*(12), 6104–6119. https://doi.org/10.1029/2018JD030100

Tanaka, H. L., Ishizaki, N., & Kitoh, A. (2004). Trend and interannual variability of Walker, monsoon and Hadley circulations defined by velocity potential in the upper troposphere. *Tellus A: Dynamic Meteorology and Oceanography*, *56*(3), 250–269. https://doi.org/10.3402/tellusa.v56i3.14410

Tang, Y., & Yu, B. (2008). An analysis of nonlinear relationship between the MJO and ENSO. *Journal of the Meteorological Society of Japan*, *86*(6), 867–881. https://doi.org/10.2151/jmsj.86.867

Totz, S., Tziperman, E., Coumou, D., Pfeiffer, K., & Cohen, J. (2017). Winter precipitation forecast in the European and Mediterranean regions using cluster analysis. *Geophysical Research Letters*, *44*(24), 418–426. https://doi.org/10.1002/2017GL075674

Trenberth, K. E., & Stepaniak, D. (2003). Seamless poleward atmospheric energy transports and implications for the Hadley circulation. *Journal of Climate*, *16*(22), 3706–3722. https://doi.org/10.1175/1520-0442(2003)016<3706:spaeta>2.0.co;2

Trenberth, K. E., Stepaniak, D. P., & Caron, J. M. (2000). The global monsoon as seen through the divergent atmospheric circulation. *Journal of Climate*, *13*(22), 3969–3993. https://doi.org/10.1175/1520-0442(2000)013<3969:tgmast>2.0.co;2

Wang, C., Deser, C., Yu, J.-Y., DiNezio, P., & Clement, A. (2017). El niño and southern oscillation (ENSO): A review. In P. W. Glynn, D. P. Manzello, & I. C. Enochs (Eds.), *Coral reefs of the eastern tropical pacific: Persistence and loss in a dynamic environment* (pp. 85–106). Springer. https://doi.org/10.1007/978-94-017-7499-4_4

Wheeler, M., & Hendon, H. (2004). An all-season real-time multivariate MJO index: Development of an index for monitoring and prediction. *Monthly Weather Review*, *132*(8), 1917–1932. https://doi.org/10.1175/1520-0493(2004)132<1917:aarmmi>2.0.co;2

Wheeler, M., & Kiladis, G. N. (1999). Convectively coupled equatorial waves: Analysis of clouds and temperature in the wavenumber-frequency domain. *Journal of the Atmospheric Sciences*, *56*(3), 374–399. https://doi.org/10.1175/1520-0469(1999)056<0374:ccewao>2.0.co;2

Wilks, D. (2011). *Statistical methods in the atmospheric sciences*. Academic Press.

Zhang, C. (2005). Madden-Julian oscillation. *Reviews of Geophysics*, *43*(2). https://doi.org/10.1029/2004RG000158

Zhang, G., & Wang, Z. (2013). Interannual variability of the Atlantic Hadley circulation in boreal summer and its impactss on tropical cyclone activity. *Journal of Climate*, *26*(21), 8529–8544. https://doi.org/10.1175/JCLI-D-12-00802.1